ACS APPLIED MATERIALS & INTERFACES

Research Article

www.acsami.org

Real-Time, Selective Detection of Pb^{2+} in Water Using a Reduced Graphene Oxide/Gold Nanoparticle Field-Effect Transistor Device

Guihua Zhou, Jingbo Chang, Shumao Cui, Haihui Pu, Zhenhai Wen, and Junhong Chen*

Department of Mechanical Engineering, University of Wisconsin-Milwaukee, 3200 North Cramer Street, Milwaukee, Wisconsin 53211, United States

ABSTRACT: A field-effect transistor (FET) device-based sensor is developed to specifically detect Pb^{2+} ions in an aqueous environment that is notably toxic. Reduced graphene oxide (rGO), as the semiconducting channel material, was utilized in the FET device through a self-assembly method. An L-glutathione reduced was employed as the capture probe for the label-free detection. By monitoring the electrical characteristics of the FET device, the performance of the sensor was measured and investigated. Compared with conventional detection technologies, this sensor enabled real-time detection with a response time of 1−2 s. A lower detection limit for Pb^{2+} ions as low as 10 nM was achieved, which is much lower than the maximum contaminant level for Pb^{2+} ions in drinking water recommended by the World Health Organization. Furthermore, the rGO FET sensor was able to distinguish Pb^{2+} from other metal ions. Without any sample pretreatment, the platform is user-friendly.

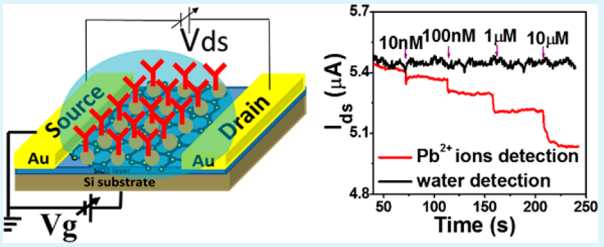

KEYWORDS: *graphene oxide, gold nanoparticle, field-effect transistor, Pb^{2+} detection*

INTRODUCTION

Lead, to a certain degree, is a poisonous substance to animals and humans. Lead poisoning has been documented since ancient Rome, ancient Greece, and ancient China. Recently, there have been numerous reports on the leaching problem of lead from water piping systems to drinking water,[1,2] which has become a health threat, especially for young children and infants. Excessive lead damages the central nervous system and causes brain and blood disorders in mammals.[3] Lead has the ability to form complex with ligands of biological matters that contain nitrogen, sulfur, and oxygen. As the covalent interaction between filled ligand orbitals (e.g., O 2p) and the Pb^{2+} $6s^2$ and empty 6p orbitals could create bonding and antibonding molecular orbitals (MOs).[4] Further, the complex leads to changes in the molecular structure of proteins, breaking of hydrogen bonds, and inhibition of enzymes.[5] Therefore, it is important to develop rapid, sensitive and low-cost methods to *in situ* detect lead ions in the drinking water efficiently and effectively to prevent lead poisoning.

Traditional methods to detect heavy metal ions include graphite furnace atomic absorption spectroscopy (GFAAS),[6] cold vapor generation,[7] and an ion chromatograph pretreatment system with inductively coupled plasma emission spectroscopy (ICPES).[8] Recently, many methods have been proposed to detect Pb^{2+}; these methods include atomic absorption spectrometry,[9,10] fluorescent sensors,[11,12] colorimetric sensors,[13,14] electrochemical sensors,[15] and X-ray absorption fine structure spectroscopy,[16] and ultrasensitive dynamic light scattering assays.[17] Although significant progress has been made for these methods, there are still some critical issues to be addressed, for example, lack of portability, the need for well-trained personnel, highly expensive and complex instruments, long response time (tens of minutes, hours, or even longer), and the possibility of introducing additional contamination. Therefore, it is highly desirable to develop a real-time, low-cost, portable, user-friendly analytical platform for rapid inline analysis of lead and other heavy metal ions.

Recently graphene-based sensing platforms have been reported for the detection of various analytes.[18−21] Graphene is a two-dimensional crystal composed of pure carbon, with sp^2-bonded carbon atoms arranged in a regular hexagonal pattern.[22] Graphene shares the outstanding properties of a carbon nanotube (CNT), including high electron mobility, excellent thermal conductivity and mechanical strength, and exceptional surface-to-volume ratio.[23,24] In addition, graphene exhibits many unique properties, such as high capacitance, exceptionally low-noise electron mobility,[25] and tunable ambipolar field-effect characteristics.[26] The high electron mobility[18] makes graphene highly sensitive to the external environment, enables its potential applications for gas sensors, biosensors, and heavy metal ion sensors.

Although graphene synthesis has been improved over the years,[27,28] its production cost is still relatively high. A less expensive alternative to graphene is reduced graphene oxide (rGO), which is a derivative of graphene and can be produced by chemically or thermally reducing GO. Various methods have been reported to synthesize GO.[21] Generally these methods involve the oxidation of graphite to graphite oxide using the

Received: August 6, 2014
Accepted: October 9, 2014
Published: October 9, 2014

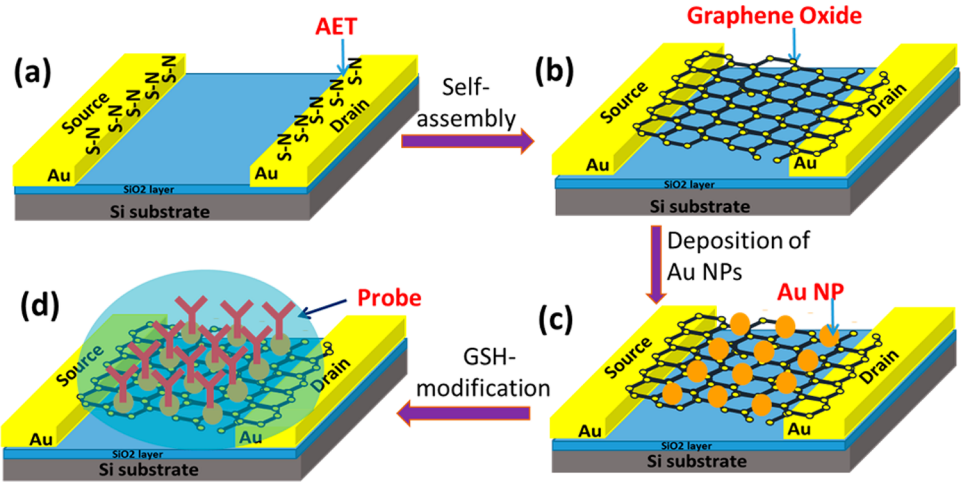

Figure 1. Schematic diagram of the rGO/GSH-Au NP hybrid sensor fabrication process. (a) A layer of AET coating on the bare interdigitated electrode surface. (b) Self-assembly of GO monolayer sheets on the AET-modified electrodes, which is followed by the thermal reduction of GO to rGO. (c) The assembly of Au NPs onto the rGO film. (d) GSH-modification of Au NPs on the rGO sheet surface to form specific recognition groups to detect Pb^{2+}.

modified Hummers method,[29] which is followed by exfoliation of graphite oxide to form GO. GO differs from graphene in its rich oxygen-containing surface functional groups. Because of its inherent oxygen-containing functional groups (e.g., epoxy, hydroxyl, and carboxyl), rGO can be easily functionalized with various probes.[20,30] For example, Sudibya et al.[31] designed a field-effect transistor (FET) sensor using protein-functionalized rGO films. The electrical conductivity of the rGO changed promptly upon the metal ion binding due to the interaction between the protein probe and the rGO film. By taking advantage of excellent electrical properties of rGO, the device exhibited a high sensitivity toward metal ions at concentrations as low as 1 nM.

In this report, we introduce an rGO/L-glutathione reduced (GSH)−Au nanoparticle (NP) hybrid structure for water sensor applications. The fundamental mechanism is to use rGO as the conducting channel to transport charge carriers (electrons or holes). Upon the capture of target analytes, the charge carrier concentration and/or the electronic mobility change correspondingly with a signal of current change within the channel. The FET characteristic changes upon the introduction of the Pb^{2+} solution, varies with different Pb^{2+} concentrations ranging from 10 nM to 10 mM, and only takes a few seconds to respond. Ag^{+}, As^{5+}, Cd^{2+},Cu^{2+}, Hg^{2+}, Zn^{2+}, and their mixed ions were used to verify the selectivity of the rGO/GSH-Au NP hybrid sensor to Pb^{2+}. The rapid, selective, sensitive, and stable detection performance indicates the promise of rGO/GSH-Au NP hybrid sensors for Pb^{2+} detection in an aqueous solution.

EXPERIMENTAL METHODS

Material. Purified natural graphite was purchased from SP-1. Bay Carbon, MI. $KMnO_4$, $NaNO_3$, H_2SO_4, GSH, α-ethyl-tryptamine (AET), and the blocking buffer (0.1% Tween 20) were all purchased from Sigma-Aldrich. Au NPs were sputtered with an RF (60 Hz) Emitech K550x sputter coater apparatus using an Au target. Ag^{+}, As^{5+}, Cd^{2+},Cu^{2+}, Hg^{2+}, Zn^{2+}, and Pb^{2+} solutions were prepared by adding chloride salts in deionized (DI) water (Cellgro). The assays of Pb^{2+} in our experiments were characterized using the inductively coupled plasma (ICP) method. The ICP analysis result was 20% higher than the calculated experimental sample concentration.

GO was synthesized using the modified Hummer's method.[30] First, the purified natural graphite was oxidized through treatment with $KMnO_4$ and $NaNO_3$ in concentrated H_2SO_4 (Sigma-Aldrich).[29] Because of the presence of its inherent oxygen-containing functional groups, graphite oxide has excellent water solubility, strong hydrophilicity, and a facile surface-functionalization feature; thus, it can be fully exfoliated in water to form graphene oxide (GO). Then, the GO dispersion was centrifuged to remove possible agglomeration materials. Finally, with the assistance of ultrasonication, individual GO sheets were obtained from the stable suspension.[32]

Device Fabrication. To guarantee the electronic stability of the device, we used an electrostatic self-assembly method to control the uniformity of the GO film. In this method, an amino-terminated Au electrode was employed to anchor the GO. Figure 1a,b illustrates the chemical anchoring procedure of a monolayer AET film. The electrode was immersed in an AET (1 mg/mL) solution for 10 min to adsorb a monolayer of AET onto the electrodes, as shown in Figure 1a. When immersing the electrode in the GO solution, GO sheets self-assembled onto the electrode, as illustrated in Figure 1b. One droplet of the GO suspension was pipetted onto the electrode and dried at room temperature (~25 °C). Single GO layer was attached onto the electrode, and excessive GO was removed with the assistance of sonication. Thermal reduction was conducted in a tube furnace (Lindberg Blue, TF55035A-1) by heating the device for 1 h at 400 °C. After the thermal heating, samples were spontaneously cooled to room temperature. Several cycles of washing and drying were carried out. Figure 1c,d shows the deposition of Au NPs onto the rGO surface and the functionalization of Au NPs with GSH probes.[4] Here we deposited Au NPs for 2 s using an RF (60 Hz) Emitech K550x sputter coater apparatus using an Au target (99.999% purity), at an Ar pressure of 0.03 mbar and a working current of 10 mA. A uniform Au NP film of 2 nm thickness resulted, as shown in Figure 1c. The Au NPs were functionalized with GSH groups by immersing the device in a 10 mM GSH solution at 25 °C for 12 h. Then the sensor was rinsed with DI water for several times to remove extra GSH and dried with a stream of nitrogen gas. A self-assembled monolayer of GSH was formed on the gold surface, as shown in Figure 1d. Finally, the device was incubated with a blocking buffer for 2 h at room temperature and washed with the DI water. A three-terminal FET device was employed to measure the device transport characteristics. The drain current (I_{ds}) was measured as a function of the gate voltage (V_{gs}) and a function of the drain voltage (V_{ds}), with the gate bias varying from −40 to +40 V.

Measurement. Electrical and transport measurements were performed on rGO/GSH-Au NP hybrid structure sensors using a Keithley 4200 semiconductor characterization system, with a back-gate applied to the FET device at room temperature. By measuring the

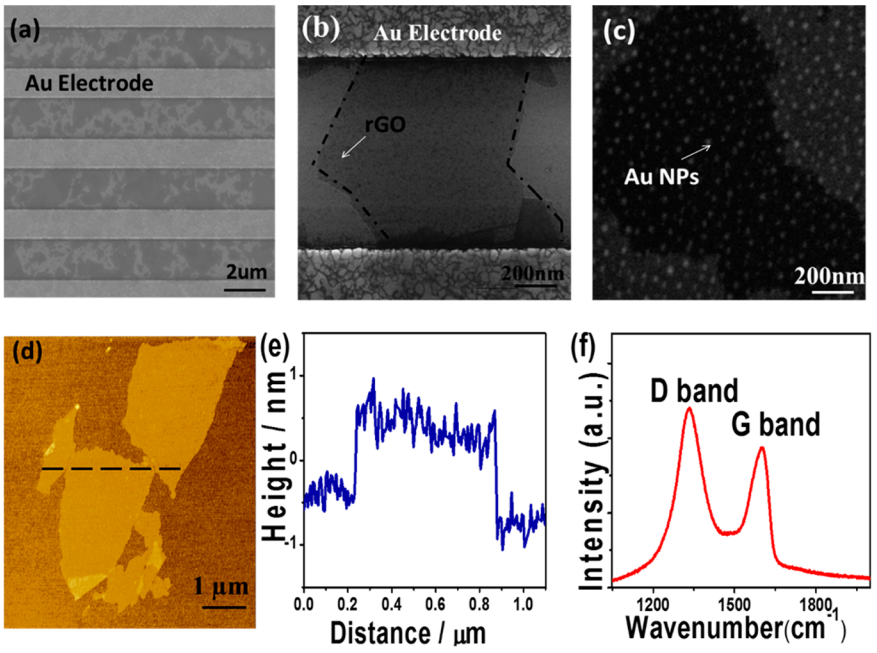

Figure 2. (a, b) SEM images of rGO sheets spanning across the interdigitated electrodes, showing transparency to the electron beam. (c) SEM image of the rGO sheet decorated with Au NPs of 2 nm thick. (d, e) Atomic force microscopy (AFM, tapping mode) height image and profile of rGO with the dashed line indicating the scanning trace. (f) Raman spectrum of the rGO.

change in the electrical characteristics of the device, we achieved the electrical detection of the target agent that was bound to the probes. The electrical conductance of the device was recorded by monitoring the change in the drain current (I_{ds}) for a fixed source−drain voltage (V_{ds}) when the device was exposed to different concentrations of target solutions. To further confirm the sensor repeatability, the detection process was repeated using 3−4 sensors, which showed similar sensing responses.

Characterization. The morphology of the rGO sheets was characterized by a Hitachi S4800 field-emission scanning electron microscope (SEM) at a 2 kV acceleration voltage. Figure 2a shows the SEM image of a transparent rGO sheet spanning across a pair of Au interdigitated electrodes. The Au interdigitated electrodes are about 2 mm long and 50 nm thick, with both finger-width and interfinger spacing that separates the source and drain terminals around 2 μm. The electrodes were fabricated using a photolithographic process on a highly doped Si wafer with an upper layer of dry-formed SiO_2 (thickness of 200 nm). Normally, GO is electrically insulating with a resistance on the order of tens of gigaohms. The high resistance results from the abundant saturated sp^3 bonds and high density of electronegative oxygen atoms bonded to carbon atoms. SEM imaging was periodically conducted, which suggested the reliable immobilization of rGO sheets on the electrodes. Lateral dimensions of rGO typically ranged from several hundred nanometers to several micrometers, as shown in Figure 2b. When the Au NPs were sputtered, isolated Au NPs uniformly distributed on the surface of the rGO sheet without any aggregation, as shown in Figure 2c. It was the physical adsorption between Au NPs and rGO that retained the Au NPs on the rGO surface even after several cycles of rinsing in deionized water and drying. Figure 2d,e shows an AFM image and a height profile of rGO, by scanning from bare silicon substrate surface to rGO. The film thickness was estimated as ∼1 nm, corresponding with the typical thickness of a single-layer graphene oxide sheet (∼0.8 nm),[33] which suggested that the GO film in our sample was monolayer. Raman spectrum for the rGO in Figure 2f shows that the D band is higher than the G band, indicating the abundance of defects in the rGO.[34]

RESULTS AND DISCUSSION

AET adsorbed onto the Au electrode surface through the strong affinity of sulfur in the thiol functional groups.[35] On one hand, the electrostatic adsorption between functional groups (e.g., carboxylic acid) on the GO surface and amino groups of the AET[36] enabled the first GO layer to strongly adhere to AET. On the other hand, because of the weak binding between additional layers and the first layer next to the electrode, excessive GO layers were removed through sonication.

Thermal annealing was conducted to remove residue solvents, reduce the GO sheets, improve the contact, and reduce the junction barrier between the Au electrode and GO sheets. Argon at a flow rate of 0.6 L per minute is necessary to create an anaerobic atmosphere and to reduce oxygen-containing groups. Hence the Au electrode and rGO sheets work as the conducting channel for the sensor device. The conductance of the rGO was dependent on annealing temperature, annealing time, and annealing gaseous environment.[37] After the self-assembly of rGO, we need to create anchoring sites for immobilizing probes. Here Au NPs were chosen because their excellent functionalization can be used to improve the sensor performance.[38] The pre-existing abundance of thiolated groups on Au NPs allowed the incorporation of a wide range of molecules onto the surface of the GO sensor.[39]

In the present study, GSH links with Au NPs through −SH linkage.[40] The TEM imaging and UV−visible spectroscopy[17] of GSH-modified Au NPs have been reported. GSH has two free −COOH groups and one $-NH_2$ group, which provide a hydrophilic interface and a handle for functionalization with metal ions.[13] The complexation between GSH and Pb^{2+} in an aqueous solution has previously been studied by ^{13}C and ^{1}H NMR methods within a pH range 5.4−12.0.[41] A blocking buffer (BB) was employed to shield the interaction between the rGO and Pb^{2+}, as anions of rGO would have electrostatic interactions with Pb^{2+}, affecting the specific interaction between Pb^{2+} and GSH.

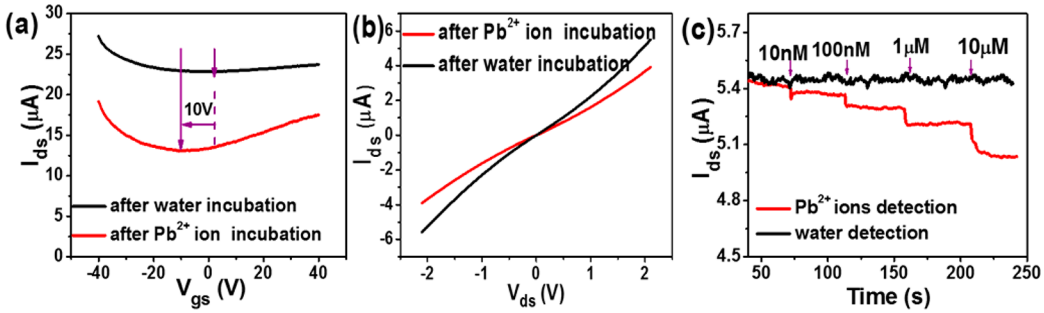

Figure 3. (a) I_{ds}–V_{gs} (V_{ds} = 5 V, V_{gs} = −40 to 40 V, step = 0.2 V). (b) I_{ds}–V_{ds} (V_{ds} = −2.1 to 2.1 V, step = 0.1 V) characteristics of an rGO/GSH-Au NP hybrid sensor exposed to water (black) and 10 μM Pb^{2+} solution (red). (c) Real-time detection (V_{ds} = 0.1 V) of Pb^{2+} in water with the rGO/GSH-Au NP hybrid sensor. Lower detection limit: 10 nM (0.002 mg/L).

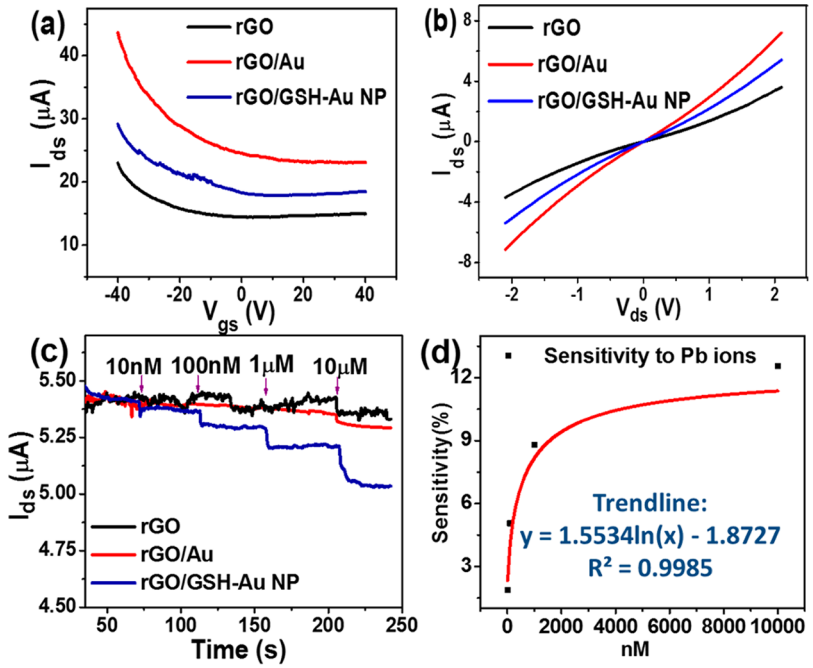

Figure 4. (a) I_{ds}–V_{gs} (V_{ds} = 5 V, V_{gs} = −40 to 40 V, step = 0.2 V). (b) I_{ds}–V_{ds} (V_{ds} = −2.1 to 2.1 V, step = 0.1 V) characteristics of various devices. (c) I_{ds} vs time (V_{ds} = 0.1 V) (dynamic responses) of rGO-based sensing platforms: rGO (black), rGO/Au (red), rGO/GSH-Au NP (blue). (d) The sensitivity trendline of the rGO/GSH-Au NP hybrid sensor to Pb ions ranging from 10 nM to 10 μM: $y = 1.5534 \times \ln(x) - 1.8727$, $R^2 = 0.9985$.

The sensor was exposed to DI water with 10 μM Pb^{2+}, and Pb^{2+} affected the conductivity of the rGO/GSH-Au NP hybrid sensor. The channel conductance changed sensitively due to the electron donating and withdrawing effect of target ions. In this FET device, a positive gate voltage leads to a depletion layer by repelling the positively charged holes away from the gate-insulator/semiconductor interface, thus producing a carrier-free region of immobile and negatively charged acceptor ions. Here, Au NPs work as the gate in the FET device.[42] Because of the effective electronic transfer between the rGO and Au NPs, the adsorption of target ions onto probes may lead to a carrier concentration change in rGO. As shown in Figure 3a, the Dirac point of the sensor shifted by approximately −10 V because of the immobilization of Pb^{2+} ions. The negative shift of the Dirac point can be attributed to the field effect of positive Pb^{2+} on the graphene channel. In the p-channel depletion-mode FET device, once the metal ions bond to the hybrid sensor, the positive electrical field of the Pb^{2+} will force the holes away from the gate-insulator/semiconductor interface, leading to a difference in the charge carrier concentration within rGO sheets, a decrease of the hole concentration in the rGO sheet, and the formation of a depletion layer,[43] which consequently causes the reduction of the electrical conductivity of the rGO channel in the rGO-FET device. Therefore, compared with water, the exposure to Pb^{2+} reduced the electrical conductance through the hole-transport branch of the graphene device.

Figure 3c shows the dynamic response of the rGO/GSH-Au NP hybrid sensor as a function of Pb^{2+} concentration ranging from 10 nM to 10 μM. During the cumulative addition of Pb^{2+} to the sensor, the drain current versus time was monitored. The sensor responded within a few seconds to the Pb^{2+} due to the diffusion of ions from the liquid drop on the top of the device to the contact area. This is much faster than conventional fluorescence sensors, which take minutes or even hour.[34,44,45]With the cumulative addition of the Pb^{2+} solution, the conductance of the device decreased gradually, and the rate of the decrease, or percentage change, was in direct proportion to the concentration of Pb^{2+}. The lower detection limit is 10 nM, defined as the concentration corresponding with a signal-to-noise ratio of approximately 3,[11] and it is 5 times lower than

the MCL for Pb^{2+} ions in drinking water defined by the WHO.[46]

We designed a control experiment to investigate the function of Au NPs and GSH probes in the hybrid-sensing platform. As shown in Figure 4, three types of sensors were fabricated. The first was the bare rGO device without decorating any Au NPs or GSH-functionalized Au NPs. Figure 4c shows that the device did not respond to Pb^{2+} ions, implying that there was no significant binding between rGO and Pb^{2+}. The second sensor was fabricated with rGO and Au NPs without the functionalization of GSH probes. As Figure 4c shows, the rGO Au-NPs hybrid device was insensitive to the presence of Pb^{2+}. In the third device, rGO film was modified with GSH-functionalized Au NPs, which was highly sensitive to the addition of Pb^{2+}.

In Figure 4a,b, the typical electrical characteristics, namely, the $I_{ds}-V_{gs}$ and $I_{ds}-V_{ds}$ curves, of these three types of sensors are presented. The deposition of Au NPs enhanced the drain current of the rGO film, which could be attributed to two competing factors. On one hand, comparing the work function of Au NPs (5.1−5.47 eV) and rGO (4.4−4.65 eV),[47] electrons would transfer from the rGO to the Au NPs, increasing the density of holes in the rGO film and thereby increasing the drain current. The other factor is that when Au NPs are sputtered onto the rGO film, they enlarged the scattering center across the film and hence reduced the mobility of the holes of the film and leading to a decrease in the drain current. According to the increased drain current, it can be inferred that the electron transfer mechanism dominated in this case. However, the assembly of negatively charged GSH molecules onto Au NPs weakened the drain current enhancement that was introduced by the deposition of Au NPs, possibly because GSH was negatively charged, and negative charges would transfer from GSH to rGO. Overall, the drain current of the rGO/GSH-Au NP hybrid sensor increased compared with the GO device. Compared with the pure rGO film sensing platform and the sensor fabricated with an rGO film and Au NPs, the assembly of a stable GSH-functionalized Au NP structure onto an rGO-based platform could achieve excellent Pb^{2+} detection, according to the electrical characteristics and the dynamic response (Figure 4c).

To explore the specificity of the GSH probe to Pb^{2+}, we monitored the dynamic response of the hybrid sensor to several mineral elements that are necessary for human health.[48] As Figure 5 shows, the sensor response to Na^+ and Ca^{2+} is rather weak. However, when exposed to Fe^{3+}, the sensor conductivity showed some changes, which may result from the strong affinity of Fe^{3+} to carboxylic groups on rGO.[49] However, the interference of Fe^{3+} is obvious only when its concentration exceeds 1 μM, suggesting that rGO/GSH-Au NP hybrid sensor is still selective to Pb^{2+}, with the Fe^{3+} at a concentration lower than 1 μM.

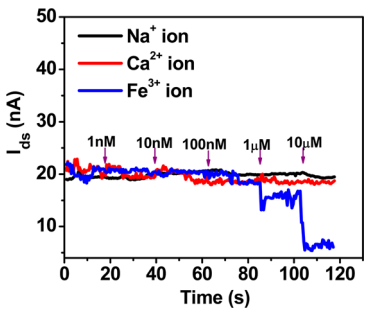

Figure 5. Dynamic responses (V_{ds} = 0.36 mV) of the rGO/GSH-Au NP hybrid sensor to common metal ions: Na^+, Ca^{2+}, Fe^{3+}.

To further confirm the specificity, we also investigated the behavior of the hybrid sensor when it was exposed to a variety of common heavy metal ions: Ag^+, As^{5+}, Cd^{2+},Cu^{2+}, Hg^{2+}, Pb^{2+}, Zn^{2+}, and mixed solution of these six kind of ions (10 μM). The I_{ds} characteristics and relative current changes are presented in Figure 6a,b. Compared with the significant responses of Pb^{2+} and the ion mixture, the responses of the hybrid sensor to Ag^+, As^{5+}, Cd^{2+},Cu^{2+}, Hg^{2+}, and Zn^{2+} ions were much weaker, due to the fact that amidogen, thiol, and carbonyl groups of GSH favor binding with Pb^{2+}. The increasing relative change can be attributed to the decreasing hole concentration in the rGO sheet.[43] As suggested by the previous work, the positively charged holes are forced away from the gate-insulator/semiconductor interface by the positive electrical field of the Pb^{2+}, and the hole concentration in the rGO sheet decreases. As a result, a depletion layer is created, leading to the conductance change in the rGO-FET device.

With the development of advanced biochemical, electrochemical, physical detection technologies, various methods have been created for the detection of Pb^{2+}, with significant progress being made in the lower detection limit. For example, the colorimetric sensor of GSH-functionalized Au NPs had a lower detection limit of 100 nM,[13] and catalytic beacon-based fluorescent sensor with functional DNAzyme had a lower detection limit of 10 nM.[50] In the fluorescent method, the lower detection limit of the GO/aptamer quantum dot (QD) sensor was 0.09 nM.[11] An electrochemical SnO_2/rGO sensor based on FET had a lower detection limit of 0.184 nM,[51] the lower detection limit of an electrochemical sensor with nafion-graphene reached 0.003 nM.[52] An rGO-FET sensor got the detection limit of 0.02 nM.[53] These achievements are listed in Table 1. However, besides the lower detection limit, response time and portability need to be addressed. Compared with other sensors, our graphene-based FET sensor can provide the detection result in a few seconds instead of tens of minutes or even longer, which makes the real-time detection feasible. At present, we are aiming at the sensitive detection of target ions, and the sensor is for one-time use only. The sensing device can be reused for three times with the rinse of acidic buffer (pH = 2.8), and no significant degradation in the sensitivity was observed. As reported previously, this type of hybrid sensors has great potential for reuse if a proper method can be identified to detach target ions from the probes.[18,31] For real applications of the rGO/GSH-Au NP hybrid sensor, it is necessary to further investigate the reusability and the stability.

CONCLUSION

In summary, a real-time, sensitive, specific, user-friendly, portable, and low-cost sensor, using an rGO/GSH-Au NP hybrid structure, has been developed for the detection of Pb^{2+}. The detection is enabled by recording the electrical conductance of the device through monitoring the change in the drain current of the rGO sheets decorated with GSH-functionalized Au-NPs. The monolayer GO sheets were selectively deposited onto the electrodes by a self-assembly method and were thermally annealed to enhance their contact with the Au electrode. The experimental results show that Pb^{2+} can be detected quickly (1−2 s) and sensitively with a lower detection limit of 10 nM. The sensor is also selective against

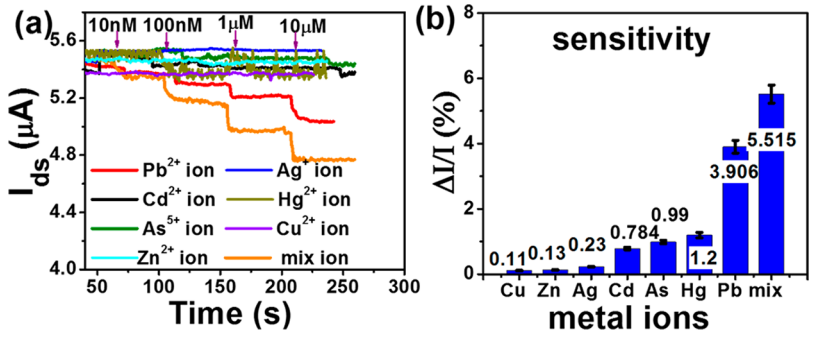

Figure 6. (a) Dynamic responses (V_{ds}= 0.1 V) to varying concentrations of heavy metal ions and (b) relative current change of an rGO/GSH-Au NP hybrid sensor in response to various heavy metal ions: Ag^{+}, As^{5+}, Cd^{2+},Cu^{2+}, Hg^{2+}, Pb^{2+}, Zn^{2+}, and mixed solution of the six ions (10 μM).

Table 1. Lower Detection Limit Achieved by Different Methods Measuring Lead Ions in Water

	methods	structure and materials	lower detection limit (nM)
literature review	colorimetric sensor	GSH-Au NPs	100[13,54]
	fluorescent sensor	DNAzyme	10[50]
		GO/aptamer QD	0.09[11]
	electrochemical sensor	SnO_2/rGO	0.184[51]
		nafion-graphene	0.003[52,55]
	electronic sensor	rGO-FET	0.02[53]
our work		rGO/GSH-Au NP	10

other metal ions. The platform offers a promising route for real-time, high-performance, and low-cost detection of various chemicals and bacteria in an aqueous environment.

AUTHOR INFORMATION

Corresponding Author

*E-mail: jhchen@uwm.edu.

Notes

The authors declare no competing financial interest.

ACKNOWLEDGMENTS

This work was financially supported by the U.S. National Science Foundation (NSF) through the NSF Industry/University Cooperative Research Center on Water Equipment & Policy led by the Univ. of Wisconsin-Milwaukee and Marquette Univ. (IIP-0968887) and an NSF fundamental research grant (Grant No. IIP-1128158). The authors thank Dr. H. A. Owen for technical support with SEM analyses at the UWM Electron Microscope Laboratory. The e-beam lithography was performed at the Center for Nanoscale Materials of Argonne National Laboratory, which is supported by the U.S. Department of Energy, Office of Science, Office of Basic Energy Sciences, under Contract No. DE-AC02-06CH11357.

REFERENCES

(1) Halim, C. E.; Scott, J. A.; Natawardaya, H.; Amal, R.; Beydoun, D.; Low, G. Comparison between Acetic Acid and Landfill Leachates for the Leaching of Ph(ll), Cd(ll), As(V), and Cr(VI) from Cementitious Wastes. *Environ. Sci. Technol.* **2004**, *38*, 3977−3983.

(2) Mason, S. E.; Trainor, T. P.; Chaka, A. M. Hybridization-Reactivity Relationship in Pb(II) Adsorption on Alpha-Al_2O_3-water Interfaces: A DFT Study. *J. Phys. Chem. C* **2011**, *115*, 4008−4021.

(3) Shukla, G. S.; Singhal, R. L. The Present Status of Biological Effects of Toxic Metals in the Environment: Lead, Cadmium, and Manganese. *Can. J. Physiol. Pharmacol.* **1984**, *62*, 1015−1031.

(4) Walsh, A.; Watson, G. W. The Origin of the Stereochemically Active Pb(II) Lone Pair: DFT Calculations on PbO and PbS. *J. Solid State Chem.* **2005**, *178*, 1422−1428.

(5) Aragay, G.; Pons, J.; Merkoci, A. Recent Trends in Macro-, Micro-, and Nanomaterial-Based Tools and Strategies for Heavy-Metal Detection. *Chem. Rev.* **2011**, *111*, 3433−3458.

(6) Gasparik, J.; Vladarova, D.; Capcarova, M.; Smehyl, P.; Slamecka, J.; Garaj, P.; Stawarz, R.; Massanyi, P. Concentration of Lead, Cadmium, Mercury and Arsenic in Leg Skeletal Muscles of Three Species of Wild Birds. *J. Environ. Sci. Health, Part A: Toxic/Hazard. Subst. Environ. Eng.* **2010**, *45*, 818−823.

(7) Leopold, K.; Foulkes, M.; Worsfold, P. Methods for the Determination and Speciation of Mercury in Natural Waters-A Review. *Anal. Chim. Acta* **2010**, *663*, 127−138.

(8) Ho, T. Y.; Chien, C. T.; Wang, B. N.; Siriraks, A. Determination of Trace Metals in Seawater by an Automated Flow Injection Ion Chromatograph Pretreatment System with ICPMS. *Talanta* **2010**, *82*, 1478−1484.

(9) Matocha, C. J.; Elzinga, E. J.; Sparks, D. L. Reactivity of Pb(II) at the Mn(III,IV) (oxyhydr) Oxide-water Interface. *Environ. Sci. Technol.* **2001**, *35*, 2967−2972.

(10) Vu, H. P.; Shaw, S.; Brinza, L.; Benning, L. G. Crystallization of Hematite (alpha-Fe_2O_3) under Alkaline Condition: The Effects of Pb. *Cryst. Growth Des.* **2010**, *10*, 1544−1551.

(11) Li, M.; Zhou, X. J.; Guo, S. W.; Wu, N. Q. Detection of Lead (II) with a "turn-on" Fluorescent Biosensor Based on Energy Transfer from CdSe/ZnS Quantum Dots to Graphene Oxide. *Biosens. Bioelectron.* **2013**, *43*, 69−74.

(12) Brenneman, K. L.; Poduri, S.; Stroscio, M. A.; Dutta, M. Optical Detection of Lead(II) Ions Using DNA-Based Nanosensor. *IEEE Sens. J.* **2013**, *13*, 1783−1786.

(13) Chai, F.; Wang, C. A.; Wang, T. T.; Li, L.; Su, Z. M. Colorimetric Detection of Pb^{2+} Using Glutathione Functionalized Gold Nanoparticles. *ACS Appl. Mater. Interfaces* **2010**, *2*, 1466−1470.

(14) Li, T.; Wang, E.; Dong, S. Lead(II)-Induced Allosteric G-Quadruplex DNAzyme as a Colorimetric and Chemiluminescence Sensor for Highly Sensitive and Selective Pb^{2+} Detection. *Adv. Anal. Chem.* **2010**, *82*, 1515−1520.

(15) Xu, K.; Meshik, X.; Nichols, B. M.; Zakar, E.; Dutta, M.; Stroscio, M. A. Graphene- and Aptamer-based Electrochemical Biosensor. *Nanotechnology* **2014**, *25*, 205501.

(16) Boyanov, M. I.; Kmetko, J.; Shibata, T.; Datta, A.; Dutta, P.; Bunker, B. A. Mechanism of Pb Adsorption to Fatty Acid Langmuir Monolayers Studied by X-ray Absorption Fine Structure Spectroscopy. *J. Phys. Chem. B* **2003**, *107*, 9780−9788.

(17) Beqa, L.; Singh, A. K.; Khan, S. A.; Senapati, D.; Arumugam, S. R.; Ray, P. C. Gold Nanoparticle-Based Simple Colorimetric and Ultrasensitive Dynamic Light Scattering Assay for the Selective Detection of Pb(II) from Paints, Plastics, and Water Samples. *ACS Appl. Mater. Interfaces* **2011**, *3*, 668−673.

(18) Chang, J. B.; Zhou, G. H.; Christensen, E. R.; Heideman, R.; Chen, J. H. Graphene-based Sensors for Detection of Heavy Metals in Water: A Review. *Anal. Bioanal. Chem.* **2014**, *406*, 3957−3975.
(19) Chang, J. B.; Mao, S.; Zhang, Y.; Cui, S. M.; Zhou, G. H.; Wu, X. G.; Yang, C. H.; Chen, J. H. Ultrasonic-assisted Self-assembly of Monolayer Graphene Oxide for Rapid Detection of Escherichia Coli Bacteria. *Nanoscale* **2013**, *5*, 3620−3626.
(20) Chen, K. H.; Lu, G. H.; Chang, J. B.; Mao, S.; Yu, K. H.; Cui, S. M.; Chen, J. H. Hg(II) Ion Detection Using Thermally Reduced Graphene Oxide Decorated with Functionalized Gold Nanoparticles. *Anal. Chem.* **2012**, *84*, 4057−4062.
(21) Huh, S.; Park, J.; Kim, Y. S.; Kim, K. S.; Hong, B. H.; Nam, J. M. UV/Ozone-Oxidized Large-Scale Graphene Platform with Large Chemical Enhancement in Surface-Enhanced Raman Scattering. *ACS Nano* **2011**, *5*, 9799−9806.
(22) Robinson, J. T.; Zalalutdinov, M.; Baldwin, J. W.; Snow, E. S.; Wei, Z. Q.; Sheehan, P.; Houston, B. H. Wafer-scale Reduced Graphene Oxide Films for Nanomechanical Devices. *Nano Lett.* **2008**, *8*, 3441−3445.
(23) Mandal, H. S.; Su, Z. D.; Ward, A.; Tang, X. W. Carbon Nanotube Thin Film Biosensors for Sensitive and Reproducible Whole Virus Detection. *Theranostics* **2012**, *2*, 251−257.
(24) Morton, J.; Havens, N.; Mugweru, A.; Wanekaya, A. K. Detection of Trace Heavy Metal Ions Using Carbon Nanotube-Modified Electrodes. *Electroanalysis* **2009**, *21*, 1597−1603.
(25) Bolotin, K. I.; Sikes, K. J.; Jiang, Z.; Klima, M.; Fudenberg, G.; Hone, J.; Kim, P.; Stormer, H. L. Ultrahigh Electron Mobility in Suspended Graphene. *Solid State Commun.* **2008**, *146*, 351−355.
(26) Agarwal, S.; Zhou, X. Z.; Ye, F.; He, Q. Y.; Chen, G. C. K.; Soo, J.; Boey, F.; Zhang, H.; Chen, P. Interfacing Live Cells with Nanocarbon Substrates. *Langmuir* **2010**, *26*, 2244−2247.
(27) Song, P.; Zhang, X. Y.; Sun, M. X.; Cui, X. L.; Lin, Y. H. Synthesis of Graphene Nanosheets Via Oxalic Acid-induced Chemical Reduction of Exfoliated Graphite Oxide. *RSC Adv.* **2012**, *2*, 1168−1173.
(28) Zhang, F. J.; Jang, W. K.; Oh, W. C. Synthesis and Characterization of Graphene-Based Nanosheets via Chemical Reduction of Expanded Graphite Oxide. *Asian J. Chem.* **2012**, *24*, 371−376.
(29) Marcano, D. C.; Kosynkin, D. V.; Berlin, J. M.; Sinitskii, A.; Sun, Z. Z.; Slesarev, A.; Alemany, L. B.; Lu, W.; Tour, J. M. Improved Synthesis of Graphene Oxide. *ACS Nano* **2010**, *4*, 4806−4814.
(30) Yu, K. H.; Lu, G. H.; Mao, S.; Chen, K. H.; Kim, H.; Wen, Z. H.; Chen, J. H. Selective Deposition of CdSe Nanoparticles on Reduced Graphene Oxide to Understand Photoinduced Charge Transfer in Hybrid Nanostructures. *ACS Appl. Mater. Interfaces* **2011**, *3*, 2703−2709.
(31) Sudibya, H. G.; He, Q. Y.; Zhang, H.; Chen, P. Electrical Detection of Metal Ions Using Field-Effect Transistors Based on Micropatterned Reduced Graphene Oxide Films. *ACS Nano* **2011**, *5*, 1990−1994.
(32) Stankovich, S.; Piner, R. D.; Chen, X. Q.; Wu, N. Q.; Nguyen, S. T.; Ruoff, R. S. Stable Aqueous Dispersions of Graphitic Nanoplatelets Via the Reduction of Exfoliated Graphite Oxide in the Presence of Poly(sodium 4-styrenesulfonate). *J. Mater. Chem.* **2006**, *16*, 155−158.
(33) Akhavan, O. The Effect of Heat Treatment on Formation of Graphene Thin Films from Graphene Oxide Nanosheets. *Carbon* **2010**, *48*, 509−519.
(34) Ghosh, T.; Biswas, C.; Oh, J.; Arabale, G.; Hwang, T.; Luong, N. D.; Jin, M.; Lee, Y. H.; Nam, J. D. Solution-Processed Graphite Membrane from Reassembled Graphene Oxide. *Chem. Mater.* **2012**, *24*, 594−599.
(35) Carro, P.; Torres, D.; Diaz, R.; Salvarezza, R. C.; Illas, F. Mechanisms of Defect Generation and Clustering in CH3S Self-Assembled Monolayers on Au(111). *J. Phys. Chem. Lett.* **2012**, *3*, 2159−2163.
(36) Fowler, J. D.; Virji, S.; Kaner, R. B.; Weiller, B. H. Hydrogen Detection by Polyaniline Nanofibers on Gold and Platinum Electrodes. *J. Phys. Chem. C* **2009**, *113*, 6444−6449.
(37) Gomez-Navarro, C.; Weitz, R. T.; Bittner, A. M.; Scolari, M.; Mews, A.; Burghard, M.; Kern, K. Electronic Transport Properties of Individual Chemically Reduced Graphene Oxide Sheets. *Nano Lett.* **2007**, *7*, 3499−3503.
(38) Huang, C. C.; Chang, H. T. Selective Gold-nanoparticle-based "turn-on" Fluorescent Sensors for Detection of Mercury(II) in Aqueous Solution. *Anal. Chem.* **2006**, *78*, 8332−8338.
(39) Zeng, S. W.; Yong, K. T.; Roy, I.; Dinh, X. Q.; Yu, X.; Luan, F. A Review on Functionalized Gold Nanoparticles for Biosensing Applications. *Plasmonics* **2011**, *6*, 491−506.
(40) Tehrani, Z. A.; Jamshidi, Z.; Javan, M. J.; Fattahi, A. Interactions of Glutathione Tripeptide with Gold Cluster: Influence of Intramolecular Hydrogen Bond on Complexation Behavior. *J. Phys. Chem. A* **2012**, *116*, 4338−4347.
(41) Mah, V.; Jalilehvand, F. Lead(II) Complex Formation with Glutathione. *Inorg. Chem.* **2012**, *51*, 6285−6298.
(42) Kwon, K. C.; Choi, K. S.; Kim, B. J.; Lee, J. L.; Kim, S. Y. Work-Function Decrease of Graphene Sheet Using Alkali Metal Carbonates. *J. Phys. Chem. C* **2012**, *116*, 26586−26591.
(43) Fowler, J. D.; Allen, M. J.; Tung, V. C.; Yang, Y.; Kaner, R. B.; Weiller, B. H. Practical Chemical Sensors from Chemically Derived Graphene. *ACS Nano* **2009**, *3*, 301−306.
(44) Ghosh, T.; Biswas, C.; Oh, J.; Arabale, G.; Hwang, T.; Luong, N. D.; Jin, M.; Lee, Y. H.; Nam, J. D. Solution-Processed Graphite Membrane from Reassembled Graphene Oxide. *Chem. Mater.* **2011**, *24*, 594−599.
(45) Li, M.; Zhou, X.; Guo, S.; Wu, N. Detection of lead (II) with a "turn-on" fluorescent biosensor based on energy transfer from CdSe/ZnS quantum dots to graphene oxide. *Biosens. Bioelectron.* **2013**, *43*, 69−74.
(46) Regulations - New Drinking Water Rules Announced. *Pollut. Eng.* **1999**, *31*, 14−15.
(47) Yu, Y. J.; Zhao, Y.; Ryu, S.; Brus, L. E.; Kim, K. S.; Kim, P. Tuning the Graphene Work Function by Electric Field Effect. *Nano Lett.* **2009**, *9*, 3430−3434.
(48) Shahidi, F.; Chavan, U. D.; Naczk, M.; Amarowicz, R. Nutrient Distribution and Phenolic Antioxidants in Air-classified Fractions of Beach Pea (Lathyrus maritimus L.). *J. Agric. Food Chem.* **2001**, *49*, 926−933.
(49) Wang, B.; Liao, L. M.; Huang, Q. H.; Cheng, Y. X. Adsorption Behaviors of Benzonic Acid by Carboxyl Methyl Konjac Glucomannan Gel Micropheres Cross-Linked with Fe^{3+}. *J. Chem. Eng. Data* **2012**, *57*, 72−77.
(50) Li, J.; Lu, Y. A Highly Sensitive and Selective Catalytic DNA Biosensor for Lead Ions. *J. Am. Chem. Soc.* **2000**, *122*, 10466−10467.
(51) Gao, C.; Yu, X. Y.; Xu, R. X.; Liu, J. H.; Huang, X. J. AlOOH-Reduced Graphene Oxide Nanocomposites: One-Pot Hydrothermal Synthesis and Their Enhanced Electrochemical Activity for Heavy Metal Ions. *ACS Appl. Mater. Interfaces* **2012**, *4*, 4672−4682.
(52) Georgakilas, V.; Otyepka, M.; Bourlinos, A. B.; Chandra, V.; Kim, N.; Kemp, K. C.; Hobza, P.; Zboril, R.; Kim, K. S. Functionalization of Graphene: Covalent and Non-Covalent Approaches, Derivatives and Applications. *Chem. Rev.* **2012**, *112*, 6156−6214.
(53) Wen, Y.; Li, F. Y.; Dong, X.; Zhang, J.; Xiong, Q.; Chen, P. The Electrical Detection of Lead Ions Using Gold-Nanoparticle- and DNAzyme-Functionalized Graphene Device. *Adv. Healthcare Mater.* **2013**, *2*, 271−274.
(54) Jayasena, S. D. Aptamers: An Emerging Class of Molecules that Rival Antibodies in Diagnostics. *Clin. Chem.* **1999**, *45*, 1628−1650.
(55) Willemse, C. M.; Tlhomelang, K.; Jahed, N.; Baker, P. G.; Iwuoha, E. I. Metallo-graphene Nanocomposite Electrocatalytic Platform for the Determination of Toxic Metal Ions. *Sensors* **2011**, *11*, 3970−3987.